RESEARCH ARTICLE

Flow visualization and wall shear stress of a flapping model hummingbird wing

Erik W. M. Swanton · Blake A. Vanier ·
Kamran Mohseni

Abstract The unsteady low Reynolds number aerodynamics of flapping flight was investigated experimentally through flow visualization by suspended particle imagery and wall shear stress measurement from micro-array hot-film anemometry. In conjunction, a mechanism was developed to create a flapping motion with three degrees of freedom and adjustable flapping frequency. The flapping kinematics and wing shape were selected for dynamic similarity to a hummingbird during hovering flight. Flow visualization was used to validate the anemometry observations of leading edge vortex (LEV) characteristics and to investigate the necessity of spanwise flow in LEV stability. The shear sensors determined LEV characteristics throughout the translation section of the stroke period for various wing speeds. It was observed that a minimum frequency between 2 and 3.5 Hz is required for the formation and stabilization of a LEV. The vortex strength peaked around 30% of the flapping cycle (corresponding to just past the translation midpoint), which agrees with results from previous studies conducted by others. The shear sensors also indicated a mild growth in LEV size during translation sections of the wing's motion. This growth magnitude was nearly constant through a range of operating frequencies.

1 Introduction

Although most researchers agree that existence of an attached leading edge vortex (LEV) is a significant contributor to the strong lift forces observed in flapping fliers,

E. W. M. Swanton · B. A. Vanier · K. Mohseni (✉)
Department of Aerospace Engineering Sciences,
University of Colorado, Boulder, CO 80309-429, USA
e-mail: mohseni@colorado.edu

the structure and stability methods of attached vorticity are still a point of controversy (Birch and Dickinson 2001; Bomphrey et al. 2005; van den Berg and Ellington 1997a, b; Srygley and Thomas 2002). Specifically, three major characteristics of the flow are questioned: growth of the separation bubble during each half-stroke, location and continuity of the LEV, and presence of axial flow.

Many studies have concluded that attachment of the LEV throughout translation implies that a dynamic stall condition is produced, which has been known to induce large lift forces in fixed-wing aircraft (Sane 2003). One of the first studies to investigate attached vorticity in flapping flight was by Maxworthy who was attempting to expand on the 'clap and fling' mechanisms that had been observed in wasps (Weis-Fogh 1973; Maxworthy 1979). During the 'fling' motion, he observed LEV structures that merged into tip vortices and root vortices at the ends of each wing. Both the tip and root vortices swept back and connected with the LEV from the opposing wing to create a continuous complex loop. The vortices remained attached and stable through the entire downstroke, explaining the underestimates of lift production by inviscid models. He also described a helical structure of the LEV where significant axial flow near the leading edge transported vorticity from the LEV core to the wingtips; thereby inhibiting the shedding that would be expected in a two-dimensional analysis.

More recently, van den Berg and Ellington visualized flow around a mechanical model of the flying hawkmoth, *Manduca sexta*, and demonstrated a similar LEV forming at the base of the wing and spiraling outward to join the tip vortices (Fig. 1) (van den Berg and Ellington 1997b). The LEV was helical over the wing with significant axial flow moving from a surface bound focus at the base to the connected tip vortex that swept backward (Fig. 2b). This
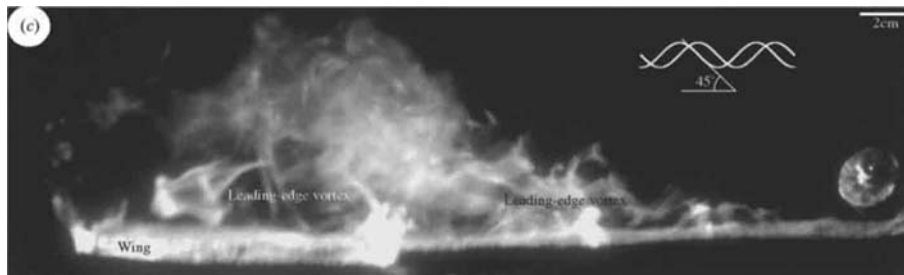
Fig. 1 Visualization of a helical leading edge vortex in a hovering model of hawkmoth indicates a strong axial flow. Smoke is released from the leading edge and moves from the base (*right*) to the tip (*left*) in an approximate 45° helix. The view is parallel to the wing chord. The image also shows an increase in LEV size with distance from the base of the wing. Figure adapted from van den Berg and Ellington (1997b)

corroborates the observations by Maxworthy, except that Ellington's single wing hovering motion could not simulate interaction with an opposing wing and thus did not recreate Maxworthy's connected root vortices. By observing smoke blobs released from the base of the wing, axial flow velocity at the middle of the wing was calculated as high as the mean velocity of the wing tip. This strong axial flow was proposed as the mechanism for maintaining the stability of LEV by bleeding energy out into the tip vortex. This similar conclusion was reached despite the order of magnitude increase in Reynolds number compared to Maxworthy's model.

While other researchers have similarly observed stable LEV structures attached to flapping wings, some have not noted the same prominent axial flow. For example, Bomphrey has questioned the role of axial flow in LEV stabilization using DPIV and smoke visualizations of a tethered hawkmoth (Bomphrey et al. 2005). The LEV was observed, but not in the helical form noted by Ellington. In fact, the LEV maintained relatively constant diameter across the entire leading edge and was continuous across the thorax (Fig. 2a). Axial flow components were not measured, but it was deduced that if axial velocity was present in the flow, it must have been <15% of the tip velocity. At this maximum value, it would be a significantly smaller percentage than the relative axial velocity found in delta-winged aircraft experiencing dynamic stall. Bomphrey suggests that the Strouhal number of the flight regime is such that vorticity does not build fast enough to be shed before the end of each stroke.

A wide variety of flapping insects have been similarly studied. Flow visualization performed by Srygley and Thomas of free flying red admiral butterflies, *Vanessa atalanta*, did not exhibit helical LEV structures, significant spanwise flow, or the increasing vortex size that is characteristic of a dynamic stall condition (Srygley and Thomas 2002). The LEV did not grow significantly throughout each stroke and was continuous across the thorax (Fig. 2a). This equilibrium without axial flow indicated that something
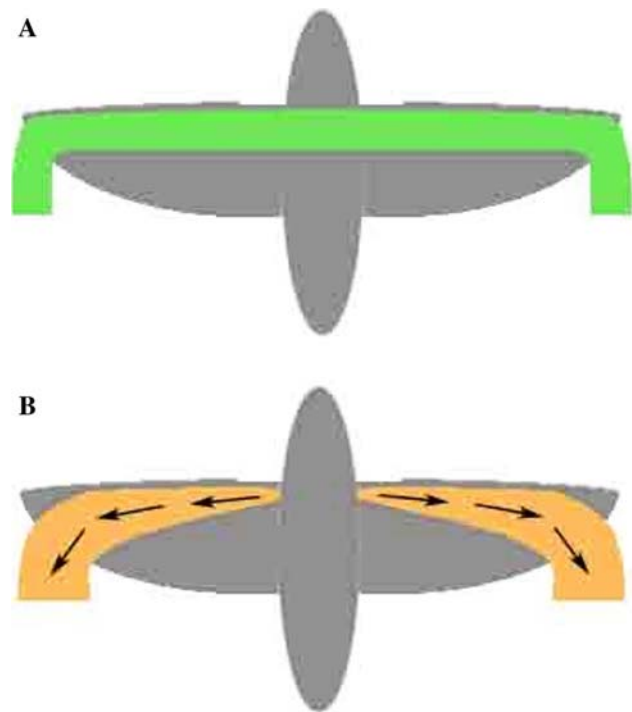

Fig. 2 Two possible LEV vortex structures proposed in literature. **a** Constant size LEV structure connecting to tip vortices and continuous between the two wings without any axial flow. **b** Helical LEV structure originating at the wing base with significant axial flow transporting vorticity away from the wing out into the tip vortices. The *arrows* show the spanwise flow inside the vortex tube

else must be stabilizing the vortex. Additionally, the butterflies employed an array of unsteady aerodynamic lift mechanisms, and an attached LEV did not appear during every stroke but only when high lift was required. Because the butterflies were flying freely in a 1.5 ms^{-1} flow instead of hovering, maximum lift was unnecessary and would have caused excessive drag. Srygley and Thomas postulated that the consistent LEV observed in tethered Hawkmoths was an artifact of the tethering and that they would likely not employ that technique during free hovering flight.

Additionally, lower Reynolds number studies by Birch and Dickinson (2001) using a robotic model of the fruit fly Drosophila did not indicate any significant axial flow, despite the presence of a stabilized LEV during downstrokes. They performed visualization of a flapping model wing where teardrop-shaped fences where mounted parallel to the chord to block axial flow. These tests indicated that bleeding vorticity from the wing tips at very low Reynolds numbers was not required to stabilize the LEV. To account for the vortex stability, they hypothesized that downwash from the tips vortices induced a decrease in effective angle of attack, which slowed the growth of LEV strength during translation. Similar to Bomphrey's later study, Birch and Dickinson concluded that the translational stroke was too brief compared to the shedding frequency and that the downwash from the tips was enough to prevent a critical buildup up vortex strength at low Reynolds numbers.

However, further study by Birch et al. (2004) directly investigated the differences between lower and higher Reynolds number flapping regimes. Extensive DPIV analysis was performed for identical wings and kinematics operating at Reynolds numbers of 120 and 1,400. The study confirmed the lack of axial flow at lower Reynolds numbers, but focused regions of significant axial flow appeared at the LEV core for the higher Reynolds number. The high Reynolds number visualizations indicated helical flow originating near the base of the wing with strong axial flow at the LEV core moving out toward the tip. The tip vortex became dominant behind the leading edge, and significant flow from tip to base was observed. The study did not replicate the fences used previously (Birch and Dickinson 2001), and it was not demonstrated whether the axial flow was necessary for LEV stability at the higher Reynolds number.

Although unique in some ways due to their coupled wing interactions, the unsteady flight mechanisms of dragonflies have also been studied extensively. Numerous studies by Saharon and Luttges (1988), Thomas et al. (2004) provide characterization of wing kinematics, LEV structure, and potential stabilization methods for both free flying dragonflies and mechanical models of the dual wing system.

Overall, most research is in agreement that attached leading edge vorticity appears during maximum lift performance of flapping flight. The mechanism of LEV stabilization is still a point of contention, but most likely some combination of axial flow, effective angle of attack, and shedding frequency allows the LEV to remain stable throughout each downstroke. In order to study these unsteady aerodynamic phenomena and their possible applications to micro aerial vehicle (MAV) flight, a versatile test bed has been built capable of mimicking hovering flight of various natural fliers. Visualization of the aerodynamic flow structures during a hovering motion along with the measurement of wall shear stress using hot-film anemometry will be used in this study.

Finding an effective tool for characterizing the unsteady flow structures over a flapping wing is a vital step toward lift control for flapping or fixed-wing MAVs. If hot-film anemometry proves an accurate method for measuring separation bubble size and qualitative vortex strength, then manipulation of LEV characteristics will be within reach. Combined with an understanding of the natural phenomena utilized by flapping fliers to maintain their high lift performance and maneuverability, synthetic mechanisms could be developed for MAV improvement. For instance, if spanwise flow was shown to be the primary stability mechanism for LEV growth, then synthetic jets could be used in conjunction with wall shear feedback to control these vital parameters of lift generation for flapping MAVs.

To present the research findings, the materials and methods will first be discussed in Sect. 2. This includes an outline of the flapping mechanism, visualization system, wing characteristics, flapping kinematics, and the shear sensors. Results and discussion take place in Sect. 3 beginning with the shear stress variation during one wing beat cycle and visual confirmation of the hot-film anemometry observations. Characteristics of the LEV are then discussed including changes with flapping frequency and variation throughout a single stroke. An analytical model for LEV shear stress is also presented relative to the experimental results. Concluding remarks can be found in Sect. 4.

2 Materials and methods

2.1 BIRDIE mechanism

In response to the need to study the low Reynolds number, unsteady, aeroelastic aerodynamics of flapping flight, a mechanism was developed called BIRDIE (Biologically Inspired low Reynolds Number Dynamic Imagery Experiment) capable of producing a variety of flapping kinematics for investigation. The mechanism employs three independent servomotors that can actuate a wing through 180° of lateral motion, 90° of vertical motion, and 360° of rotation about the wingspan axis. Existing models for the study of unsteady lift production include spinning wings that do not capture the actual flapping (Altshuler et al. 2004; Usherwood and Ellington 2002), systems that are constrained to specific frequencies (Saffman and Sheffield 1977), or perform in alternative fluids to reduce operation frequency (Birch and Dickinson 2001; Dickinson and Götz 1993; Maxworthy 1979). The BIRDIE mechanism can model nearly any complex flapping motion via three servomotors

providing three degrees of freedom. Flapping kinematics can also be changed without modifying parts of the mechanical system. Figure 3 shows the setup of the entire BIRDIE mechanism.

The BIRDIE setup consists of the visualization system, the test structure encased in polycarbonate to isolate the aerodynamics, the power delivery system for the motors, and the actual flapping mechanism (Fig. 3). The polycarbonate box measures 1.0 m × 0.8 m × 0.8 m. The right image in Fig. 3 shows a close-up of the wing mechanism and the positioning of the servomotors on the support structure.

The wing mechanism (Fig. 4a) consists of three interconnected mechanisms (rotational, vertical, and horizontal), which can be independently operated. The horizontal gimbal is the largest part of the moving mechanism and rotates back and forth to create the horizontal motion (Fig. 4b). The vertical mechanism is mounted in the horizontal gimbal and can independently rotate the wing up and down (Fig. 4c). Finally, the rotational mechanism turns inside of the vertical gimbal to create rotation along the wingspan axis (Fig. 4d).

The horizontal gimbal provides lateral motion and structural support for the entire wing mechanism (Fig. 4a). It has a direct connection to the horizontal motor using two spur gears Fig. 5. The shaft supporting the mechanism stays in place using a collar and lock nut, and the two rotary bearings allow horizontal rotation while also securing the mechanism in the stationary support structure.

The vertical gimbal is supported by the horizontal mechanism and held in place by rotary bearings to provide smooth vertical rotation (Fig. 5). A control arm connects the vertical gimbal to the gear interface mounted above on the horizontal gimbal with a linear bearing. The vertical motor drives the linear bearing up and down using a rack and pinion arrangement. This motion is transferred to the vertical gimbal through the control arm. Guides were placed on either side of the rack to ensure that the pinion
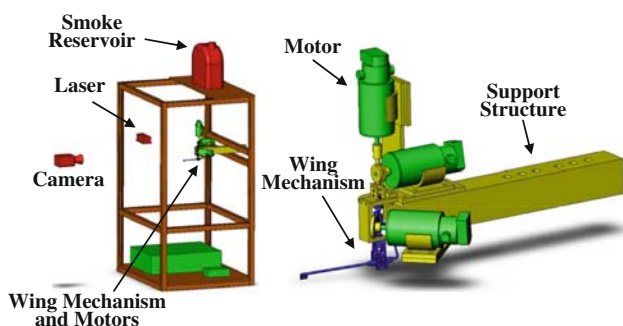

Fig. 4 The wing mechanism broken into the rotational (*orange*), vertical (*yellow*), and horizontal (*red*) mechanisms
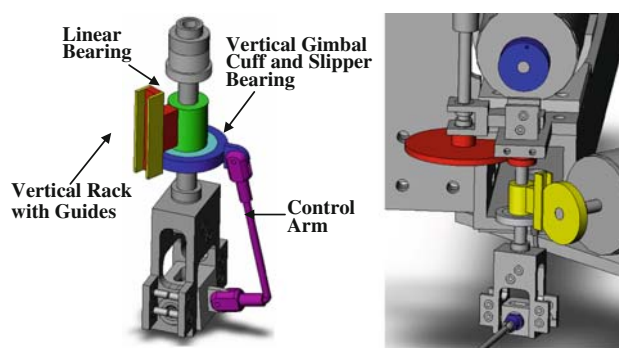
Fig. 5 *Left* Vertical and horizontal uncoupling mechanism with the control arm (*purple*), vertical gimbal cuff (*dark blue*), vertical rack (*red*) with guides (*yellow*), linear bearing (*green*), and slipper bearing (*light blue*). *Right* Wing mechanism and motor interfaces, the horizontal interface is shown in *red*, the vertical in *yellow*, and the rotational in *blue*

stays aligned when the mechanism is rotating horizontally. The slipper bearing provides horizontal freedom to the rack and pinion while the horizontal gimbal is in motion.

The rotary arm uses a Dremel collet and chuck system to allow quick interchange of wings. Cables pass through the horizontal and vertical gimbal and wrap around the rotary arm to produce motion by pulling the strings in either direction (Fig. 4d). The cable is guided through the horizontal gimbal by grooved rollers, and the ends are attached to the rotation motion motor for actuation. Cable was chosen to control wing rotation because it offers independent control with minimum complexity and weight.

This mechanism can independently rotate the wing while simultaneously moving the wing horizontally and vertically. The motor interfaces are highlighted in Fig. 5 (right). The rotational motion interface is shown in blue, with a cable connecting the pulley on the motor to the rotary arm. The yellow indicates the vertical motor interface driven by a rack and pinion. Finally, the horizontal motion is driven by two spur gears shown in red.

Fig. 3 CAD model of BIRDIE mechanism (*left*). Close-up of the wing mechanism (*blue*), support structure (*yellow*), and the motors (*green*) on the *right*
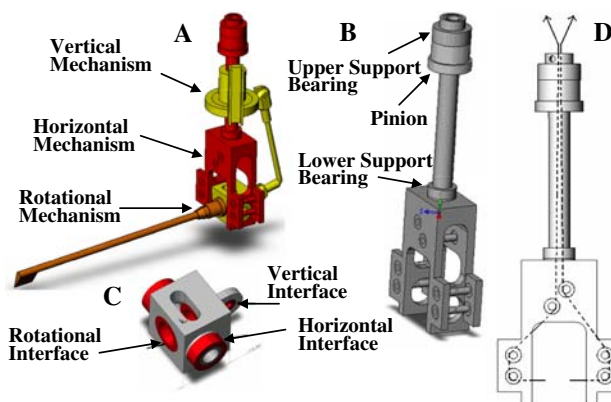
2.2 Visualization

To determine the geometry and stability of the LEV, suspended particle imagery (SPI) was employed using fine particulate oil smoke and high-speed videography. Smoke was delivered from a diffuser above the wing, creating a laminar stream of particulates across the test section.

As the wing passed through the smoke, a thin section of the wing was illuminated by a laser beam split with a beveled line-generating lens. For adequate power, an Aixiz Service and International AIX-532-1000 laser was used operating at a 532 nm wavelength and 1,000 mW. The lens was an Edmond Optics line generator with a divergence of 15° to minimize variation of the laser sheet with distance. The PS31ST Oil Based Smoke Generator provided very fine particles (0.2–0.3 micron diameter), high reflectivity, and no residue on the wing. See Fig. 6 for an image of the test setup.

Images of the visualization were gathered using a Vision Research Phantom v4.3 color high-speed camera operating between 500 and 1,200 fps depending on the flapping frequency.

2.3 Model wing and kinematics

Although insects are the most common animals capable of hovering flight, hummingbirds may provide an improved basis for investigation into MAV design due to their size, maneuverability, and lift capabilities. However, to achieve a reproducible mechanism that loosely mimics hummingbird flight, some simplifications were used to create the model wing and its associated movement. The model wing is a simple rectangular shape shown in Fig. 7, with a span of 15 cm and a chord length of 4 cm. The aspect ratio was chosen according to the average wing dimensions of the Rufus hummingbird (Tobalske et al. 2007). The matte white border was thinly painted onto the wing to increase the visibility of the edge during motion. The structure was made of a carbon fiber spar wrapped in bidirectional carbon fiber weave to produce a stiff yet light wing platform. The high stiffness was intended to reduce the possible effects of wing tip deflection. Although wing twisting and tip deflection are utilized by free flying hummingbirds, especially during pitch and roll maneuvers, a stiff wing was chosen to reduce the complexities of the model and focus on LEV stability (Warrick et al. 2005). The hot-film anemometry sensor is mounted near the base of the wing. For continuity throughout testing, all the cross-sectional structure comparisons were made 50 mm from the base of the wing (Fig. 7).

For simplicity, the mechanism was programmed so that the leading edge traced a basic figure eight shape if viewed in a plane perpendicular to the span axis. While not strictly a reproduction of hummingbird wing kinematics, the motion resembles the general hovering stroke parameters of most natural fliers.

The periodic figure eight motion was modeled using three sinusoidal functions where the vertical motion was twice the frequency of the horizontal and rotational motion (Fig. 8). The actual parameters of motion for the model were chosen based on a study of the wing kinematics of a hummingbird during hovering flight (Tobalske et al. 2007). The motion amplitudes used during testing were 70° horizontally, 20° vertically, and 70° rotationally about the wing axis. This provided a 20° geometric angle of attack during mid-downstroke, a stroke amplitude of 140°, and a

Fig. 6 Visualization test setup. The reservoir above feeds smoke through the diffuser to the test section where the wing is located. Below the test section is a second diffuser with a low suction exhaust. The image is viewed from the same position as the high-speed camera, with the laser positioned on the right and aimed into the structure
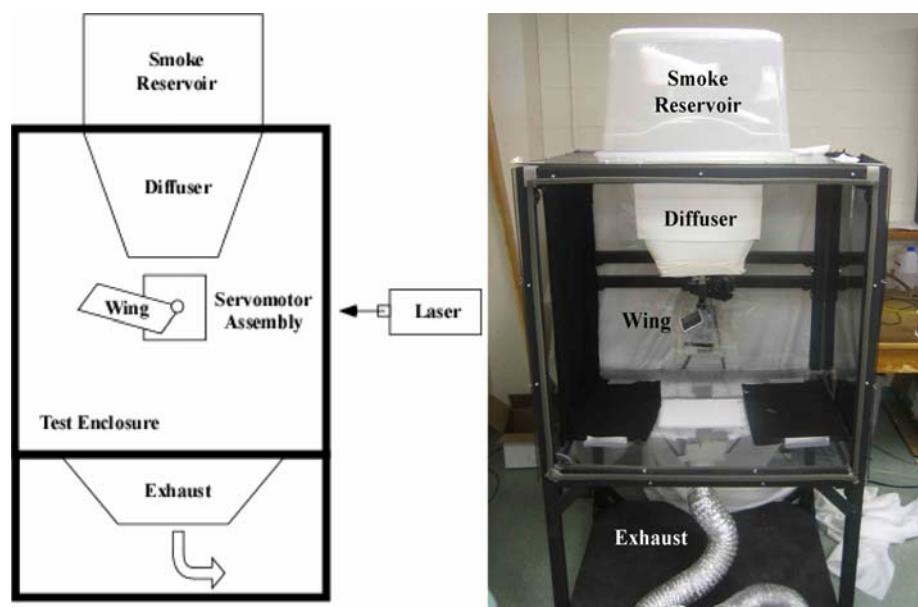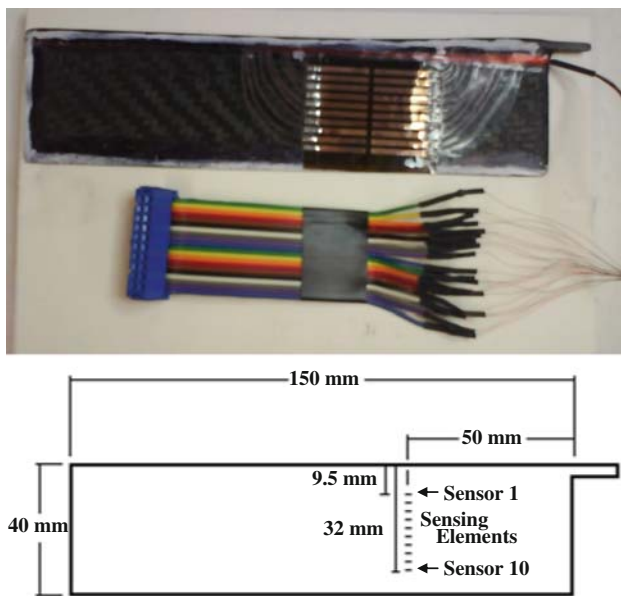
Fig. 7 *Top* Model wing with hot-film anemometer mounted at section of interested. *Bottom* Diagram of wing with and location of primary chord section of interest. The section of interest is where all cross-sectional visualizations were located, as shown in the Sect. 3
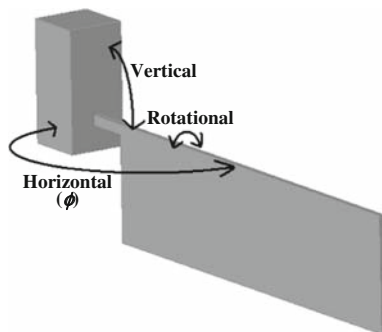

Fig. 8 Figure defining the rotations characterizing the motion

maximum stroke deviation of 20° (Sane and Dickinson 2001). For analysis of the accuracy of the mechanism in producing the proposed motion, see the work by Vanier (2008).

For hovering flight in three dimensions, using the wing tip as the reference and accounting for both the span and the cord, the Reynolds number is defined as (Shyy et al. 2008):

$$\text{Re}_{f3} = \frac{\phi f R^2}{v}\left(\frac{4}{\text{AR}}\right), \tag{1}$$

where ϕ is the amplitude of the horizontal wing motion in radians (see Fig. 8), f is the frequency, R is the wing length, v is the kinematic viscosity, AR is the aspect ratio, where $\text{AR} = (2R)^2/S$, and S is the total surface area of the wings,

and the subscript Re_{f3} represents the Reynolds number for a 3D flapping wing in hovering flight. For this study, Reynolds numbers ranged from $\sim 1{,}000$ to $5{,}100$, or very nearly 1,000 times the experimental flapping frequency.

2.4 Wall shear sensors

To provide feedback that can assist in the control of flapping flight, a sensor was selected capable of characterizing the aerodynamic flow structures over the wing. Hot-film anemometry provides a light but sensitive means of determining the size of the leading edge separation bubble through estimation of flow reattachment along the wing chord. Monitoring the evolution of the separation bubble and wall shear provides insight into lift production and therefore could enable flight control.

2.4.1 Hot-film calibration

The preliminary focus of the hot-film sensors is to detect LEV existence and any variation in the flow reattachment point; therefore, an absolute calibration is not necessary. A relative calibration of the sensors is adequate because the voltage signal from the circuit directly relates to the flow conditions. The calibration was performed by subjecting the sensors to a reference flow and then normalizing the subsequent voltage responses. All sensors are normalized relative to one reference sensor, in our case hot-film sensor number five. This ensures a similar response of each sensor, accounting for the differences in each element and the components in each constant temperature circuit. These voltages can then be used to determine the wall shear stress at any location relative to the reference hot-film sensor.

In order to generate consistent flow conditions for a normalization of the elements, a small tube provided a steady flow velocity. With the wing and sensor array secured on a platform, slides were placed to allow smooth platform movement along a fixed path. The tube was then positioned with an adjustable vice so that its exit aimed along the sensor array with a shallow angle, just a few millimeters off the wing surface.

The activated sensor array was guided under the tube at a constant velocity, the data were logged, and the procedure repeated while alternating between the front and rear sensors entering the calibration flow first. A sample result of the sensor output voltage during the calibration process is shown in Fig. 9.

Once the output spikes are captured, the baseline voltage response (with no applied airflow) is subtracted from the signal to obtain the pure response. The values are then plotted against the fifth sensor response to determine a relative scaling factor using a linear regression shown in Fig. 9.
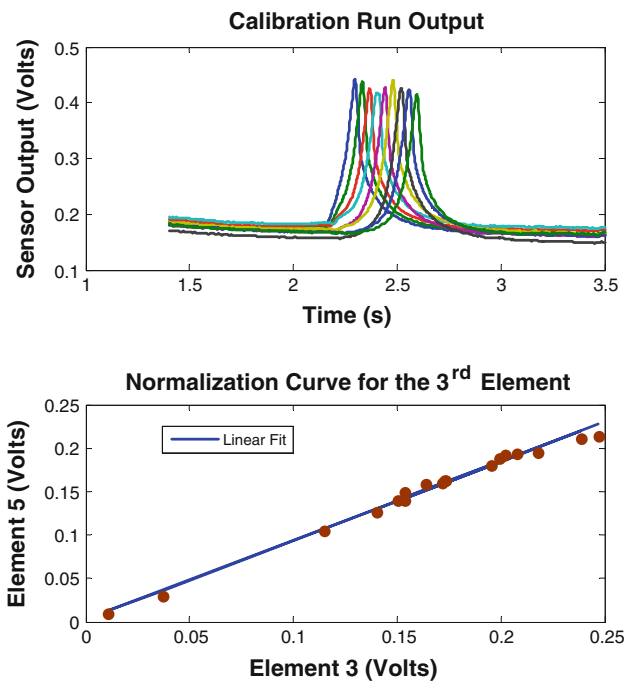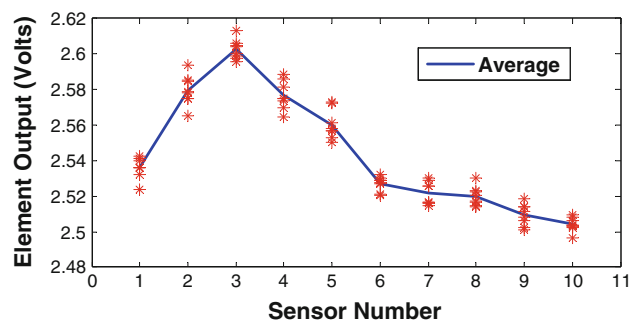
Fig. 10 A graph of the sensor voltage measurements during seven different stroke periods at 25% of the cycle. The x-axis indicates the sensor position, and the *solid line* shows the average voltage output over the cycles

$$\tau_{5,i}^{1/3} = \gamma_5 + \delta_5 V_{5,i}^2, \tag{4}$$

where γ and δ are unknown coefficients that are specific for each sensor. By factoring out δ, and using the voltage signal with no flow the ratio of δ and γ can be found as:

$$\frac{\gamma_5}{\delta_5} = -V_0^2 \tag{5}$$

Equation 4 is then referenced to values for the shear stress and voltage of the fifth sensor. The final equation is shown below.

$$\frac{\tau_{5,i}}{\tau_0} = \left(\frac{V_{5,i}^2 - V_0^2}{E_0^2 - V_0^2} \right)^3 \tag{6}$$

E_0 and τ_0 are the reference voltage and shear stress. For the full derivation see the work by Vanier (2008).

2.4.2 Post processing

The data gathered during experimentation are passed through a 125 Hz low pass filter to eliminate high frequency noise. To remove other signal variations, the voltage outputs from seven full periods are averaged together. This produces a mean signal representing the general response for a particular wing beat frequency. Figure 10 shows a curve of the averaged response for a 4 Hz motion midway through the downstroke. The data points indicate the individual voltages measured during each period. The averaged signal is then converted to a relative shear stress profile using the calibration results.

3 Results and discussion

3.1 Shear sensor signal evolution

A quick comparison of wall shear stress on the top and bottom wing surfaces indicates that some transient

Fig. 9 *Top* Calibration run, each signal spikes as it passes under the tube, which are then used to normalize their response. The first spike corresponds to the first element, with the last element at the end. *Bottom* Normalization curve for the third film element to the fifth film element

The linear fit of each element was used to normalize each signal relative to the fifth element. The normalization takes the form:

$$V_{5,i} = \alpha_i + \beta_i V_i, \tag{2}$$

where i represents the element that it is being normalized (ranging from one to ten), the five indicates the element that it is being normalized to, α is the offset, and β is the slope of the normalization. For $V_{5,5}$, α is equal to zero, and β is equal to 1. This equation now takes any voltage from one element and normalizes it to the fifth element, which ensures that all elements are behaving similarly. The modified King's law is typically used to calibrate the voltage response of a constant temperature anemometry circuit to the wall shear stress (Tavoularis 2005).

$$\frac{V^2}{T_w - T_f} = A + B\tau_w^{1/3}, \tag{3}$$

where V is the voltage output of the circuit, T_w is the temperature of the sensor, T_f is the temperature of the fluid, and A and B are coefficients established during the calibration. The offset voltage that is removed for acquisition purposes is added back into the voltages so that the modified King's law can be used properly. The modified King's law is rearranged, and the normalized voltage can be substituted in to give the normalized shear stress as:

phenomenon occurs over the top of the wing through each downstroke (Fig. 11). During the half-cycle with the sensor on top of the wing, a large increase in shear stress is observed, which disappears as the wing decelerates at the end of the stroke. This is likely due to formation of the LEV, since trapped vorticity above the wing would locally augment the shear stress. Figure 11 shows the signal evolution of the six sensors closest to the leading edge (numbers 1–6) during one full cycle at a frequency of 4 Hz. The last four sensors did not diverge significantly from the behavior of sensor 6, so they were removed for clarity.

The stroke cycle starts at point A, which is labeled on the lower figure at its position and on the upper figure at its corresponding time. The start of the top stroke occurs when the wing moves from point A to point B. The top stroke is defined as the stroke with the sensor array on the top surface of the wing. Once the wing accelerates through the top stroke, a large change in shear stress is observed as fluid moves rapidly across the top of the wing. Sensors 2, 3, and 4 report especially sharp increases in shear stress as leading edge vorticity builds and accelerates the fluid above the front of the wing. All six sensors show increases in wall shear stress as the fluid is accelerated over the top of the wing, and the sensors near the leading edge observe up to five times the stress of the rear sensors. This localized effect indicates the growth in circulation of the LEV, and as a result, increased lift production would be expected during this section of the stroke. This enhanced lift is confirmed by results from Dickinson et al. (1999). The shear stress holds through point C, where the wing starts to rotate in expectation of the bottom stroke, and then stress

begins to decrease as the wing decelerates and the vortex begins to separate with wing rotation. As the wing moves from D to E, it accelerates again, but the wing is now in the bottom stroke where the sensor is on the lower surface. The wall shear stress on the bottom of the wing increases with velocity, and there is an associated modest rise in the sensor response. However, the increase is not significant compared to the top stroke where trapped vorticity augments shear stress near the leading edge. Additionally, there is less disparity between the output signals of each sensor during the bottom stroke. This is expected as the flow remains attached to the bottom surface, and no trapped vorticity exists to produce localized spikes in the wall shear stress.

3.2 Verification of LEV detection

Using visualization of the flow during wing translation, the relative shear stress results and conclusions can be validated. Figure 12 shows sensor output and corresponding visualizations for the top stroke in the middle of the translational section. The visualizations have the corresponding signal overlaid at the appropriate position chord wise. There is a large signal spike located around the vortex followed by a rapid decrease past the reattachment point. The small dips following the large spikes could indicate a proximity to the reattachment point, where the shear stress is zero. See Sect. 3.5 for a representation of shear stress above the wing and an explanation of the expected wall shear stress over the wing.

3.3 LEV changes with frequency

To determine the behavior of the flow structures at various stroke velocities, the location of the LEV was monitored at a fixed cycle position while increasing the wingbeat frequency. This information was intended to shed light on the stability of the vortex, critical flapping frequencies, and optimal Reynolds number regimes.

Using the baseline kinematics described earlier, visualizations were collected at frequencies starting at 1 Hz and increasing to 5.5 Hz at intervals of 0.5 Hz. This corresponds to Reynolds numbers of about 1,000–5,100. The section in question was along the chord at 1/3 the half-span from the base (Fig. 7). Figure 13 shows the flow structures at half way through the downstroke for increasing frequencies. This is the position of greatest vertical and horizontal velocities with a maximum effective angle of attack.

The first two images of 1 and 2 Hz indicate that the LEV does not stabilize at low frequencies. When LEV stability is not attained, the vortices caused by leading edge separation are shed back along the chord. The periodic
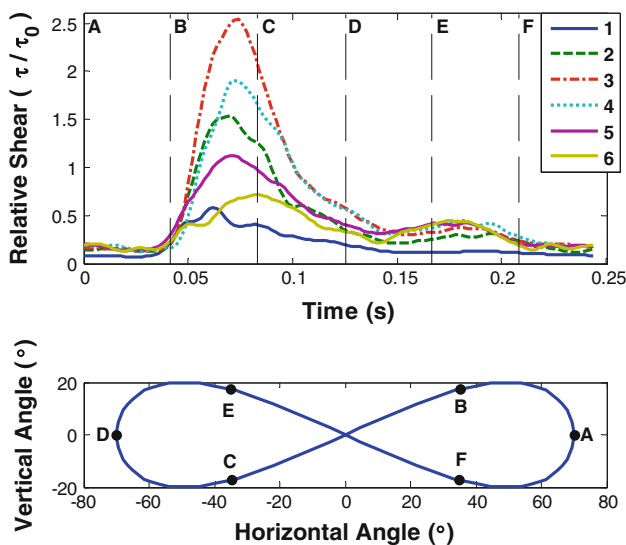

Fig. 11 *Top* Relative shear stress for hot-film sensors 1–6 vs. time over a full flapping cycle at a flapping frequency of 4 Hz. *Bottom* Shows marked points during the flapping cycle. Points *A* and *D* represent the beginning and ending of the top stroke, respectively

Fig. 12 Sensor output and
smoke visualization with signal
overlay at the middle of the top
stroke at 3.5 Hz (*top*) and at
4.5 Hz (*bottom*)
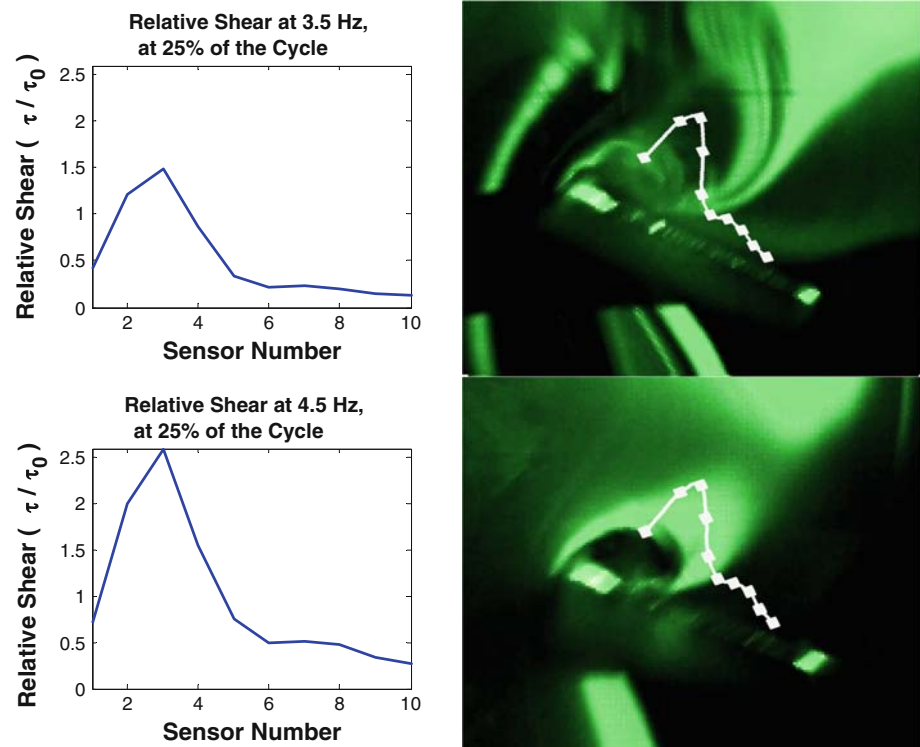
shedding of the leading edge vorticity results in an averaged chaotic region above the entire wing. At 3 Hz, vorticity begins to stabilize at the leading edge, but the structure appears disrupted along the outside of the vortex core. This instability indicates that the LEV is not completely stable and still likely to shed or be disrupted later in the stroke period. However, at 3.5 Hz, a clear LEV structure is present with far less instability around the vortex core. As frequency increases, this instability is diminished and a consistent leading edge structure appears and remains stable on the leading edge.

Figure 14 shows resulting sensor signals at 25% of the cycle for each frequency. As the frequency of the motion increases, the peaks in the shear stress increase in magnitude but remain near the same relative position. The increase in signal strength suggests that the vortex strength increase with higher flapping frequency, which is to be expected. The peaks of the signals are constant within the spatial resolution of the sensors, so the vortex location stays within ± 0.063 chord lengths for these frequencies. There is a large jump in vortex strength from 2 to 3 Hz and an even larger jump to 3.5 Hz, which agrees with the visualization that there is a minimum frequency before a stable vortex forms. However, if there is a critical frequency where vorticity builds too rapidly to stabilize, we did not reach it in our experimentation up to 6 Hz.

Interestingly, while there is an evolution of LEV stability with increasing frequency, the size of the LEV does not appear to change noticeably between the frequencies tested. Since the wing path is unchanged, a two-dimensional analysis would hypothesize increasing vorticity and augmented LEV size at higher wing speeds. However, the uniform size seems to support the existence of a mechanism that removes vorticity from the LEV, thus stabilizing a dynamic stall condition and maintaining the LEV size.

To further study the frequency influence on the LEV, the relationship of relative shear stress and the Reynolds number is examined. Equation 1 is used to calculate the Reynolds number. Because the relative shear stress and the Reynolds number both increase with frequency, the relative shear distribution divided by the corresponding Reynolds number may provide insight into the characteristics of LEV production with regard to flapping frequency. Figure 15 shows a plot of this normalized shear stress at 30% of the stroke cycle, which corresponds to the point where maximum vortex strength occurs for frequencies 1–5 Hz.

Interestingly, the maximum normalized shear increases with frequency until it peaks at 4.5 Hz, at which point the trend collapses with decreased normalized shear for 5 and 5.5 Hz. It is difficult to confidently characterize this behavior of the LEV without higher resolution shear measurements or more complex flow visualization. However, this trend should be investigated further and may provide insight into the interaction and effectiveness of certain flapping flight parameters.

Fig. 13 Visualization of the LEV at the middle of the downstroke (position *D* on Fig. 16) with increasing frequencies: 1 Hz, Re $\sim$ 920 (**a**), 2 Hz, Re $\sim$ 1,850 (**b**), 3 Hz, Re $\sim$ 2,770 (**c**), 3.5 Hz, Re $\sim$ 3,230 (**d**), 4 Hz, Re $\sim$ 3,690 (**e**), 4.5 Hz, Re $\sim$ 4,150 (**f**), 5 Hz, Re $\sim$ 4,610 (**g**), 5.5 Hz, Re $\sim$ 5,070 (**h**). The wing has been *highlighted with a white line* for easy recognition. LEV structure begins to stabilize at about 3 Hz, and then there is no significant change in vortex size through 5.5 Hz. The *blue arrow* shows the location of the first hot-film element
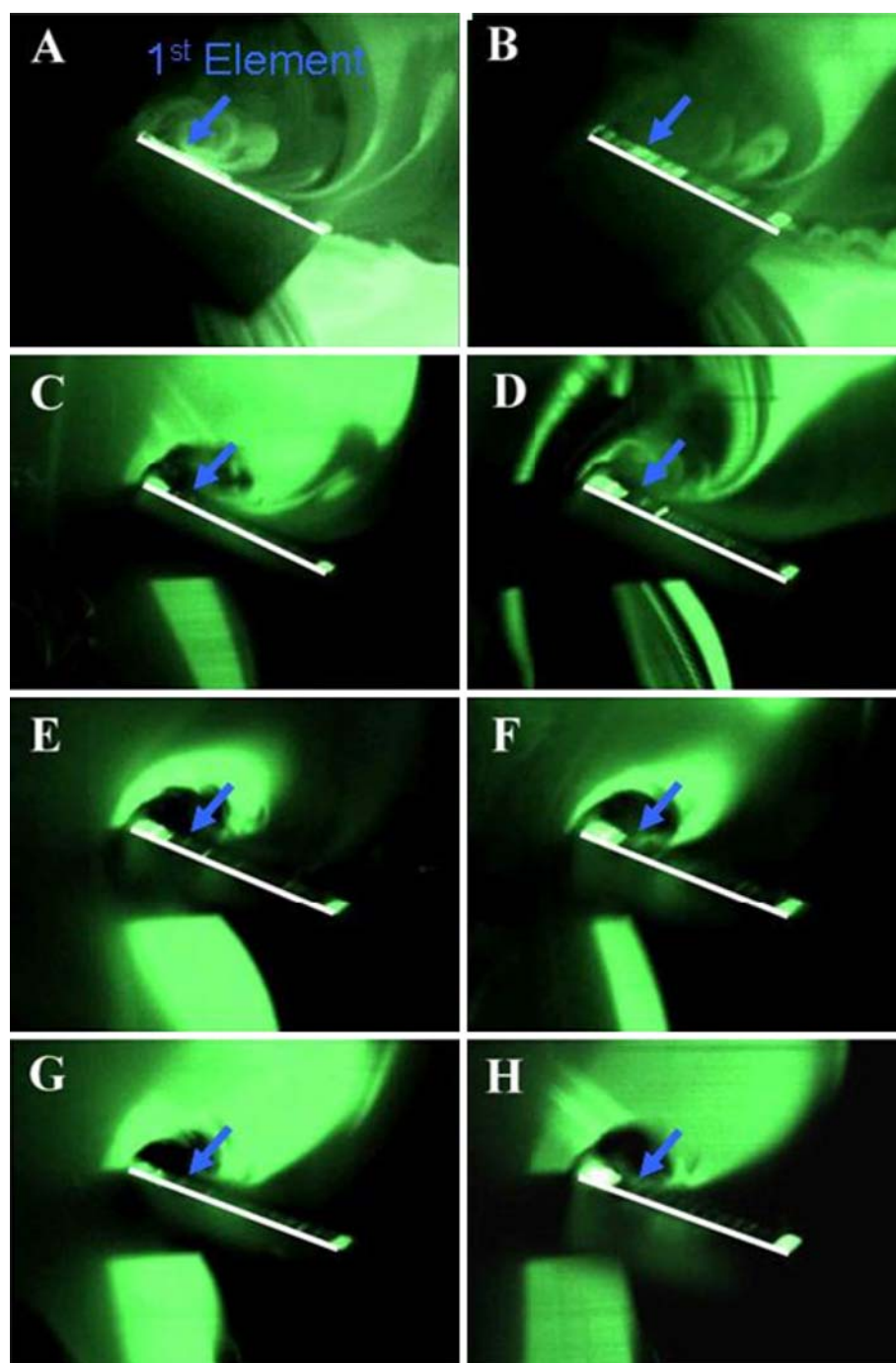
3.4 LEV growth during translation

To characterize the transient nature of the LEV, the evolution of the shear stress over the wing was observed throughout the top stroke for a 4 Hz flapping motion. Specifically, the intent was to monitor any growth or movement of the reattachment point during the translation section of the stroke. A two-dimensional analysis predicts vorticity to build during the entire downstroke, leading to growth of the separation bubble until it sheds off the back of the wing. Figure 16 shows the specific positions of the stroke cycle that were monitored for the 4 Hz frequency.

Visualization of the motion at designated positions is shown in Fig. 16. The first two images are near the beginning of the translational section (position B and C) and indicate some disturbances in the LEV during formation. This may be due to wake interactions with vorticity shed during the transition from supination to translation which has been similarly visualized in previous flapping wing experiments (van den Berg and Ellington 1997a, b).
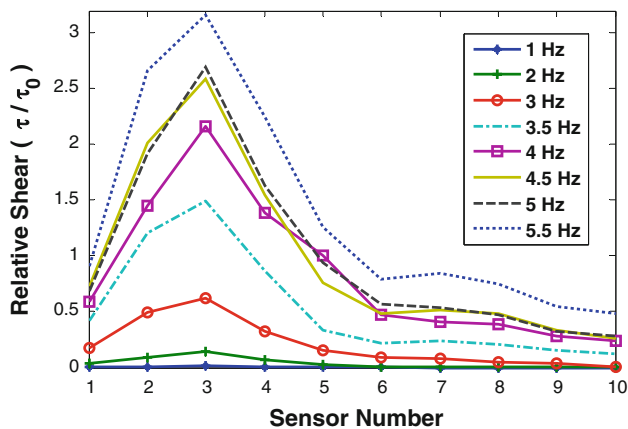
Fig. 14 Relative shear stress along the chord for various frequencies at 25% of the cycle
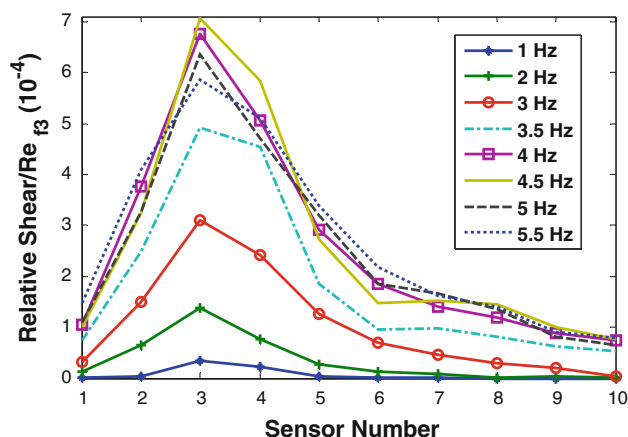

Fig. 15 Relative shear stress at different frequencies divided by the corresponding Reynolds number at 30% of the cycle

Once the LEV stabilizes, it appears to grow slightly during the translation downward. This is most clearly seen by movement of the reattachment point along the chord length. The first images show reattachment at about one-third of the chord, while this reattachment has moved nearly past the half-chord position by the end of translation. While experimental error results in some discrepancies, all visualizations indicate a gradual yet perceptible increase in vortex size throughout each downstroke. This corresponds to a slight growth in trapped vorticity between the start and end of the wing translation associated with a dynamic stall condition.

Figure 17 shows the relative shear stress measured through the stroke at the positions indicated in Fig. 16. Location A shows the beginning of the down stroke. The wall shear stress on the wing does not show significant variation along the wing, indicating that the flow is still attached to the wing. At location B, however, the shear stress along the chord becomes disrupted, likely indicating that the flow has begun to separate from the leading edge. The first

indication of LEV formation appears near location C where the wall shear stress shows a spike at the leading edge of the wing. This would be caused by trapped vorticity speeding up the flow and locally augmenting the shear. Strength of the LEV is proportional to the magnitude of wall shear stress, and the size of the LEV can be assessed by the number of sensors registering a significant disturbance. Therefore, the plots in Fig. 17 indicate an increase in strength and slight growth of the LEV between points C and F. In Fig. 11, the max strength of the LEV occurs at 30% of the cycle, and F is positioned at 31% of the cycle. Wang et al. (2004) measured the forces created by a generic hovering motion using an airfoil. Lift production of a symmetric motion was calculated from experimental and computational studies, indicating that maximum lift was near 30% of the cycle. This closely agrees with our estimated location of maximum LEV strength, which is expected since trapped vorticity greatly augments lift generation (Shyy et al. 2008). From point F toward the end of the down stroke the wing's velocity and angle of attack decreases. This corresponds to a decrease in the LEV strength. The final shedding of the LEV is associated with the drop in the magnitude of the detected wall shear stress near point K. The regularity of the signal pattern along with the corresponding visualization indicates successful detection of an attached LEV through the majority of the top stroke.

3.5 LEV wall shear stress model

The reattachment point of the LEV can be a very useful piece of information when trying to control the trapped vorticity. Because there is a forced separation point at the leading edge of the wing, the reattachment point establishes the size and position of the separation bubble. This information can be coupled with the magnitude of the wall shear stresses to provide insight into the size, strength, and stability of the LEV. To develop a model for estimating the reattachment point using hot-film sensors, the instantaneous wall shear stress was observed from direct numerical simulation of a typical flow around a low Reynolds number airfoil (Sahin et al. 2008). Figure 18 shows an instantaneous vorticity field for flow over an Eppler 387 airfoil (Sahin et al. 2008). The box at the top represents the vortex that is being considered in the bottom of the figure.

The bottom of Fig. 18 is a plot of the instantaneous coefficient of friction over the wing, where the coefficient of friction is simply the non-dimensional wall shear stress and their relationship is seen as:

$$\tau = \frac{C_f}{1/2\rho U_\infty^2}$$

where C_f is the coefficient of friction and ρ is the density of the fluid.

Fig. 16 *Top* Positions for
sequenced shear stress plots
over time, these points
correspond to 16–49% of the
cycle in 3% increments. *Bottom*
Flow visualization at 4 Hz
(Re ~ 4,000) starting at the top
of the translational section and
moving downward. *Letters*
correspond roughly to the
positions indicated in the *top*
figure. The bottom of the wing
has been *highlighted in white*
for easy visibility
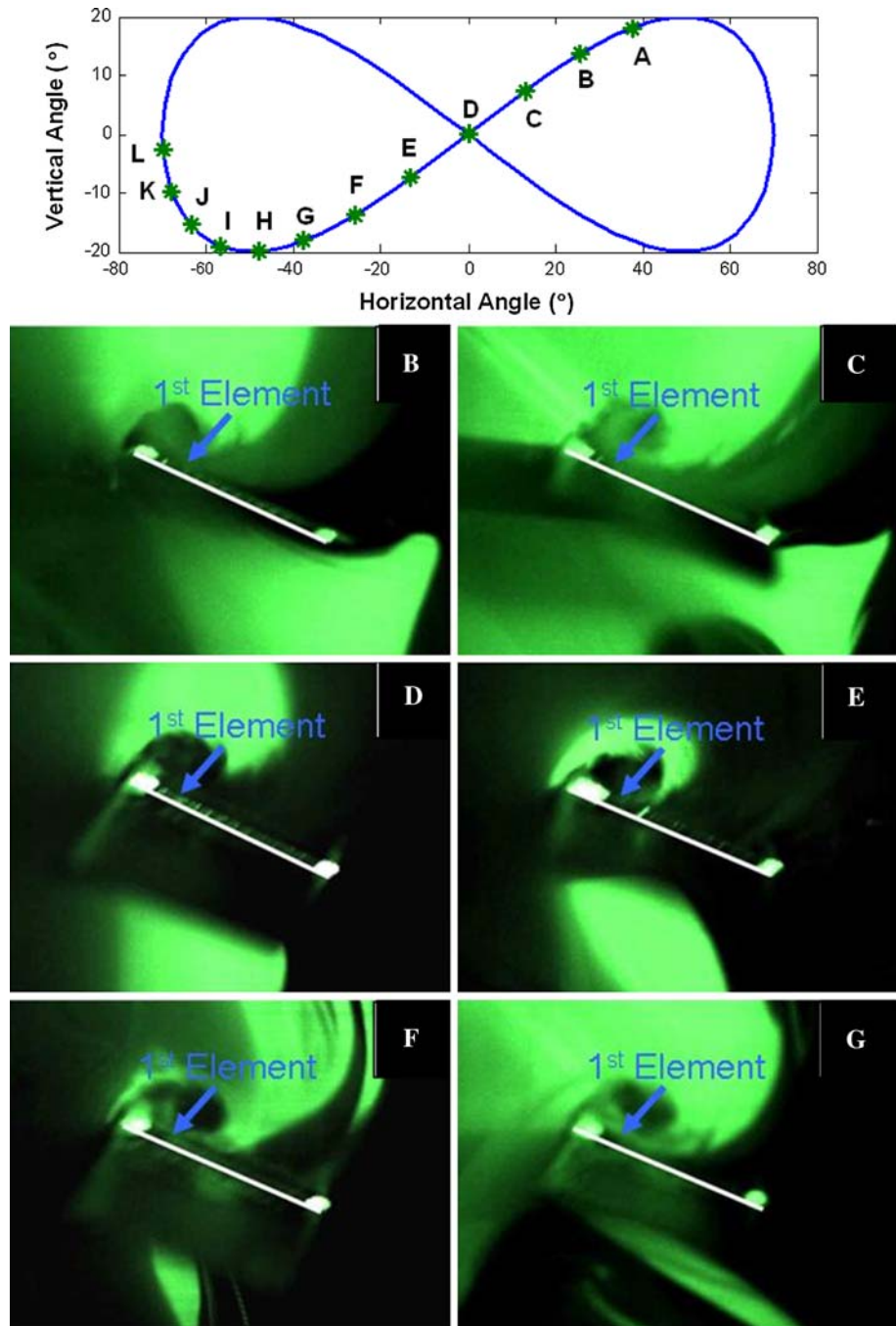
There are two attachment points of the vortex, both of which occur where the coefficient of friction is zero. In between the two attachment points, there is a large negative value as the vortex causes the flow at the wall to move in the opposite direction of the external flow velocity. Following the last attachment point, the friction value is positive as the flow over the wing is traveling in the same direction as the external flow. This behavior was used to create a model for the reattachment point over the flapping wing.

Figure 19 shows three images, a schematic of the flow streamlines near a flapping wing, an estimate of the shear stress distribution, and the absolute value of the wall shear stress. This last graph should mimic the data gathered from the hot-film sensors because they do not register flow direction.

Inside of the separation bubble, the flow near the wing will be traveling in the opposite direction of the external flow, resulting in a negative shear stress value. Toward the edges of the separation bubble the shear stress decreases, until it reaches zero. Outside of the separation bubble, the flow is traveling in the same direction as the external flow, and the shear stress is positive. The reattachment point is
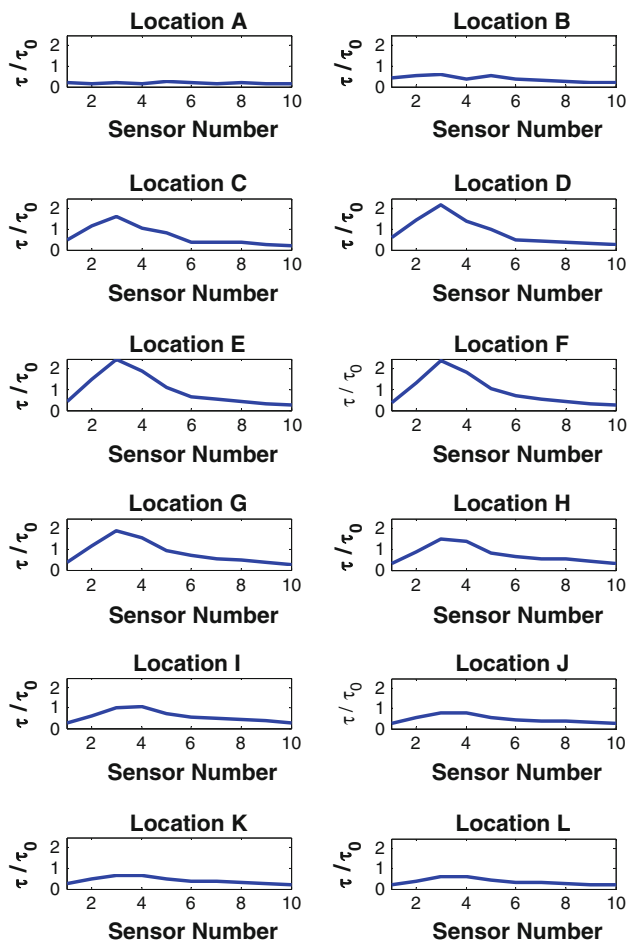
Fig. 17 Relative shear stress distribution for 4 Hz at specific positions

Fig. 19 Schematics of the LEV and wall shear stress. *Top*: typical streamlines. *Middle*: wall shear stress distribution. *Bottom*: absolute value of wall shear stress

located where the shear stress changes from a negative to a positive value. The maximum shear is located slightly aft of the center of the vortex. Because the sensors cannot differentiate the direction of the flow, both a positive and negative shear stress would look the same, as in the last image. The large peak at position a, is quite noticeable in the signal during the top stroke; however, the reattachment point at b is much harder to detect. This is due to the low spatial resolution of hot-film sensors relative to the short chord length of the wing. The simple model used here in

Fig. 18 *Top* Instantaneous vorticity field for a separated flow over an EPPLER 387 airfoil at a Reynolds number of ∼60,000 at an angle of attack of 6°. Figure compliments of Sahin et al. (2008). *Bottom* Instantaneous friction coefficient over airfoil depicted in Fig. 22. Figure adapted from Sahin et al. (2008)
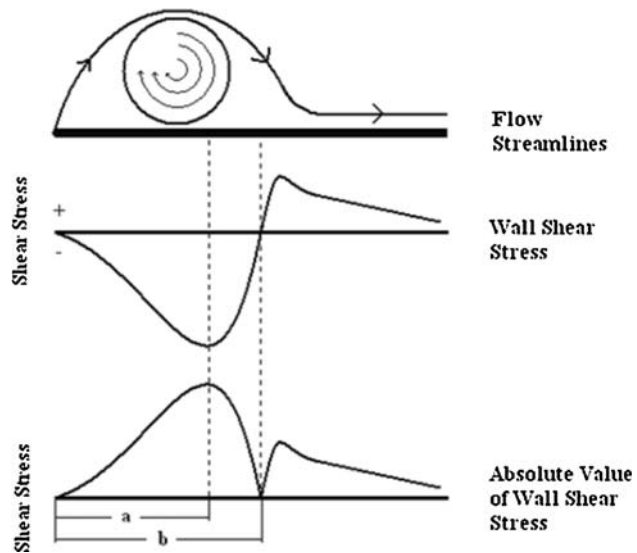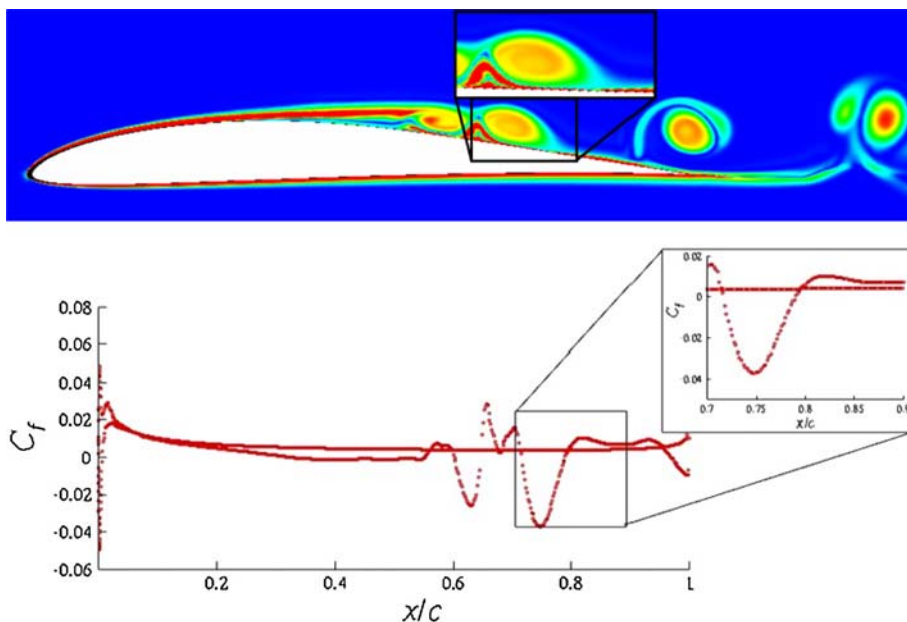
order to determine the reattachment point assumes that the ratio of *a* and *b* is constant regardless of the vortex size. This ratio was determined experimentally by analyzing flow visualizations with a visible reattachment point and comparing them with the measured shear distribution. The peak point in the signal was determined and then fit to a parabolic curve with the adjacent sensor reading. The maximum value of the parabolic curve is then taken as position *a*. Comparing with the reattachment position in the visualization, the ratio *b/a* was calculated to be 1.22. Because this type of analysis is particularly sensitive to the signal and noise level, a linear regression was fit to each signal to show the trend of reattachment behavior. The calculated reattachment points are plotted in Fig. 20 against non-dimensional time, which is time divided by the flapping frequency of the associated data. The graph indicates slightly increasing trends in vortex size through the translational stroke for all frequencies. Although precise qualitative observations of these growth rates may require more refined measurement of the reattachment point, the evolving shear distribution consistently demonstrates an increasing trend in LEV size for all testing frequencies during translation. The growth of the LEV supports the hypothesis that a dynamic stall condition exists where attached vorticity is building during translation but never reaches the critical strength to shed from the trailing edge. This phenomenon has been studied in fixed-wing aircraft and is associated with significant increase in lift production for a brief time (Shyy et al. 2008). Dynamic stall conditions are known to appear when wings travel at high angles of attack but vorticity is still bound to the top of the wing (Shyy et al. 2008). While this gives insight into the behavior of the trapped vorticity, the source of the LEV stability is still in question.
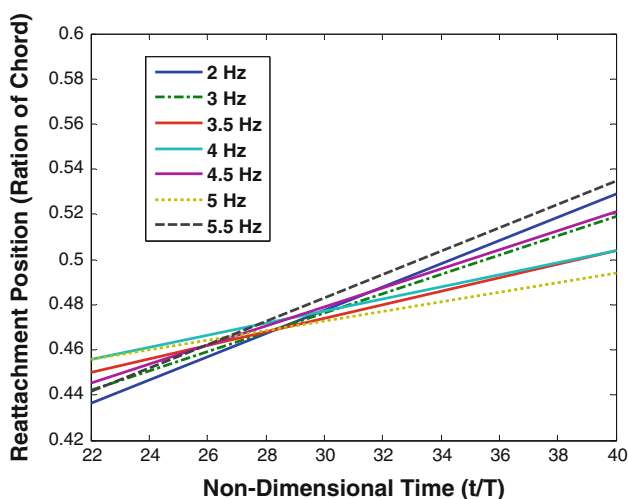

Fig. 20 Modest growth trends in LEV size during each downstroke. The location of the reattachment point during the translational part of the top stroke for frequencies 2, 3, 3.5, 4, 4.5, and 5 Hz

4 Conclusions

Flow visualization confirmed wall shear observations of LEV characteristics in higher Reynolds number flapping regimes. Hot-film anemometry and smoke particle visualization successfully monitored the appearance of a sustained LEV that has been observed in previous studies. During the translational section of the wingbeat, the LEV creates a separation bubble where the reattachment point slightly increases throughout the downstroke. However, the LEV size does not appear to change significantly at a given stroke position when the wingbeat frequency increases from 3 to 5.5 Hz. The consistent characteristics of the LEV despite increasing stroke frequency and wing velocity implies that some mechanism exists that is capable of removing vorticity and inhibiting shedding of the LEV.

An array of hot-film anemometry sensors has proven its ability to identify aerodynamic structures over a flapping wing. The hot-film sensors were used with a constant temperature circuit. These normalized voltages were then used to determine a relative wall shear stress distribution over the wing. The relative wall shear stress distribution confirmed the existence of an attached LEV associated with flapping motion. The max strength of the vortex was shown to occur at 30% of the cycle, which closely agrees with the location of the maximum lift at 29% found by Wang et al. (2004) when looking at a generic hovering motion of an airfoil.

By validating the ability to predict separation bubble size and maximum vortex strength, hot-film anemometry proves to be a potential tool for LEV control and lift optimization of flapping MAVs. The translational section of the stroke cycle is thought to produce the majority of lift for MAV-sized animals (Warrick et al. 2005), so aerodynamic feedback during this section would be extremely useful for flight control. Coupled with an improved understanding of wing rotation characteristics, control of this complicated flight regime may be possible.

References

Altshuler DL, Dudley R, Ellington CP (2004) Aerodynamic forces of revolving hummingbird wings and wing models. J Zool Proc Zool Soc Lond 264:327–332

Birch JM, Dickinson MH (2001) Spanwise flow and the attachment of the leading-edge vortex on insect wings. Nature 412:729–733

Birch JM, Dickson WB, Dickinson MH (2004) Force production and flow structure of the leading edge vortex on flapping wings at high and low Reynolds numbers. J Exp Biol 207:1063–1072

Bomphrey RJ, Lawson NJ, Harding NJ, Taylor GK, Thomas ALR (2005) The aerodynamics of Manduca sexta: digital particle image velocimetry analysis of the leading-edge vortex. J Exp Biol 208:1079–1094

Dickinson MH, Götz KG (1993) Unsteady aerodynamic performance of model wings at low Reynolds numbers. J Exp Biol 174:45–64

Dickinson MH, Lehmann FO, Sane SP (1999) Wing rotation and the aerodynamic basis of insect flight. Science 284:1954–1960

Maxworthy T (1979) Experiments on the Weis-Fogh mechanism of lift generation by insects in hovering flight. Part 1. Dynamics of the 'fling'. J Fluid Mech 93:47–63

Saffman PG, Sheffield JS (1977) Flow over a wing with an attached free vortex. Stud Appl Math 57:107–117

Saharon D, Luttges MW (1988) Visualization of unsteady separated flow produces by mechanically driven dragonfly wing kinematics model. AIAA J 88-0569:1–23

Sahin M, Hall J, Mohseni K (2008) Direct numerical simulation of separated low-reynolds number flows around an Eppler 387 Airfoil. 46th AIAA Aerospace Sciences Meeting and Exhibit. Reno, NV, 7–10 Jan 2008

Sane SP (2003) The aerodynamics of insect flight. J Exp Biol 206:4149–4208

Sane SP, Dickinson MH (2001) The control of flight force by a flapping wing: lift and drag production. J Exp Biol 204:2607–2626

Shyy W, Lian Y, Tang J, Viieru D, Liu H (2008) Aerodynamics of low Reynolds number flyers. Cambridge University Press, New York

Srygley RB, Thomas LR (2002) Unconventional lift-generating mechanisms in free-flying butterflies. Nature 420:660–664

Tavoularis S (2005) Measurement in fluid mechanics. Cambridge University Press, New York

Thomas LR, Taylor GK, Srygley RB, Nudds RL, Bomphrey RJ (2004) Dragonfly flight: free-flight and tethered flow visualizations reveal a diverse array of unsteady lift-generating mechanisms, controlled primarily via angle of attack. J Exp Biol 207:4299–4323

Tobalske BW, Warrick DR, Clark CJ, Powers DR, Hedrick TL, Hyder GA, Biewener AA (2007) Three-dimensional kinematics of hummingbird flight. J Exp Biol 210:2368–2382

Usherwood JR, Ellington CP (2002) The aerodynamics of revolving wings (I. Model hawkmoth wings). J Exp Biol 205:1547–1564

van den Berg C, Ellington CP (1997a) The vortex wake of a 'hovering' model hawkmoth. Phil Trans R Soc Lond B 352:317–328

van den Berg C, Ellington CP (1997b) The three-dimensional leading-edge vortex of a 'hovering' model hawkmoth. Phil Trans R Soc Lond B 352:329–340

Vanier B (2008) Detection of aerodynamic flow structures during hummingbird like flapping motion using hot film anemometry tavoularix. Master's Thesis. University of Colorado at Boulder

Wang ZJ, Birch JM, Dickinson MH (2004) Unsteady forces and flows in a low Reynolds number hovering flight: two-dimensional computations vs. robotic wing experiments. J Exp Biol 207:449–460

Warrick DR, Tobalske BW, Powers DR (2005) Aerodynamics of the hovering hummingbird. Nature 435:1094–1097

Weis-Fogh T (1973) Quick estimates of flight fitness in hovering animals, including novel mechanisms for lift production. J Exp Biol 59:169–230